A NEW ALGORITHM OF 3D IMAGE RECONSTRUCTION OF RADAR TARGETS FROM RAMP RESPONSES IN LOW FREQUENCY

J. Chauveau and N. de Beaucoudrey

IREENA, Université de Nantes
La Chantrerie, rue C. Pauc, Nantes 44306, France

Abstract—Low frequency imaging in radar domain can have applications for stealthy or buried targets. The transient scattering response from a ramp waveform is related to the profile function of the target, namely its transverse cross-sectional area along the line-of-sight, and thus provides information about the target size, orientation and geometrical shape. Such ramp responses can be used to generate a 3-dimensional image of the global shape of the target. Former imaging algorithm uses approximate limiting surfaces and is therefore limited to single convex objects. Here is proposed a new algorithm able to reconstruct non-convex as well as separated targets, from their ramp response signatures.

1. INTRODUCTION

Among radar targets identification problems, the scattering characterization of stealthy targets is a relevant topic. The stealthiness is intended to produce a very weak radar return and this can be obtained by using composite materials, which absorb electromagnetic waves in usual radar frequency bands. But, this can be countered by using lower frequencies. Moreover, the use of low frequency bands is very important in the case of Ground Penetrating Radar (GPR) applications for characterization of buried targets, since the wave attenuation in most soil increases with the frequency. These lower frequency bands correspond to the Rayleigh region and the resonance region for object dimensions respectively small and of the same order, compared to electromagnetic wavelengths. Contrary to high frequency imaging, low frequency methods cannot provide high resolution but they still bring

useful information on the overall dimension and approximate shape of the target.

Three dimensional (3D) microwave imaging usually requires a considerable number of directions of the incident wave for image reconstruction by inverse scattering methods, such as inverse Born approximation [1], diffraction tomography [2, 3], Bojarski method [4], etc. On the contrary, a method proposed by Young [5], known as the ramp response technique, needs no more than 3 viewing angles to generate an image. As first suggested by Kennaugh and Moffatt for radar identification [6], it uses transient scattering responses from a target illuminated by a time domain ramp waveform. In such case, the backscattered field is directly related to the transverse cross-sectional area of the target as a function of the distance along the line-of-sight. This interesting property is used for generating a 3D image of the target shape: the original algorithm of Young [5] uses "approximate limiting surfaces", supposed to enclose the unknown target, and it gives an estimate of the target shape by iteratively fitting some geometrical parameters. This ramp response imaging algorithm has been applied to electromagnetic scattering problems [5–15] as well as to acoustic imaging of underwater objects [16, 17]. However, Young's algorithm can be used only for convex and single objects [5]. That is why we propose a new algorithm permitting to reconstruct objects with arbitrary shape, as well as separated objects.

We first present, in Section 2, the ramp response and the profile function. Then, in Section 3, we describe our new algorithm for reconstructing 3D target image from ramp profile functions. In Section 4, we apply this new algorithm to realistic profile functions obtained from simulated transient responses of various objects.

2. RAMP RESPONSE AND PROFILE FUNCTION OF A TARGET

First of all, we introduce the ramp response and the profile function of a target and we explain how they are related.

2.1. Ramp Response

The ramp response of a radar target is defined as the far zone scattered wave resulting from illumination by a plane electromagnetic wave with a time domain ramp waveshape. In time domain, the ramp response of a target, $h_r(t)$, is merely the second integral of its impulse response, $h_i(t)$. It can be expressed as the Inverse Fourier Transform (IFT) of the scattered transfer function, $H(j\omega)$, weighted by $1/(j\omega)^2$ ($\omega = 2\pi f$

being the angular frequency)

$$h_r(t) = IFT\left[H_r(j\omega)\right] = IFT\left[\frac{H(j\omega)}{(j\omega)^2}\right] \tag{1}$$

Thus, the ramp response emphasizes the lower frequency components of the target scattered response.

2.2. Profile Function

First, we define the "geometrical" profile function of an object, in the x direction, as its transverse cross sectional area, $A_g(x)$, along x

$$A_g(x) = \int_{-\infty}^{+\infty} \int_{-\infty}^{+\infty} O(x,y,z)dydz \tag{2}$$

with

$$O(x,y,z) = \begin{cases} 1 \text{ if } (x,y,z) \text{ inside object} \\ 0 \text{ if } (x,y,z) \text{ outside object} \end{cases}$$

where $O(x,y,z)$ is a binary object function.

Figure 1 presents the exact, "geometrical", profile function of a target, $A_g(x)$, calculated as the area of transverse slices of the target at successive positions along x.
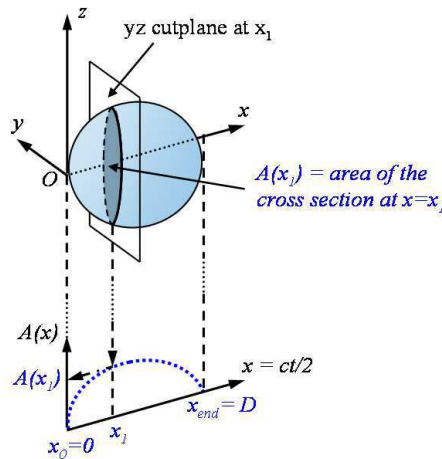

Figure 1. Illustration of the geometrical profile function of an object along x direction, $A_g(x)$. D is the characteristic dimension of the object in x direction.

In monostatic configuration, the ramp response of a target illuminated in x direction, $h_r(t)$, is approximately proportional to the geometrical profile function, $A_g(x)$, of the target [6]

$$h_r(t) \approx -\frac{1}{\pi c^2} A_g(x) \quad \text{with} \quad x = \frac{ct}{2} \tag{3}$$

where c is the speed of light in freespace, t the time variable, and x the space variable.

Indeed, Kennaugh and Moffatt [6] have established this relationship in the illuminated region of the target, using the physical optics approximation. Later, Young [5] have empirically shown that it is still valid in lower frequency bands and for the whole object, even in the shadow region with a slight loss in accuracy.

From (3), we define now the "physical" ramp profile function $A_p(x)$ as

$$h_r(t) = -\frac{1}{\pi c^2} A_p(x) \tag{4}$$

To ensure that $A_p(x)$, given by (4), is a valid estimate of $A_g(x)$, given by (2), it is necessary to match the frequency band to scatterer dimensions. From [5–8], it is required to choose the upper Rayleigh region and the resonance region of the target, corresponding to electromagnetic wavelengths included between $D/2$ and $200D$, where D is the characteristic dimension of the target in the incident direction. Thus, the corresponding required frequency band is

$$f = [f_{\min}; f_{\max}] = \left[\frac{c}{200D}; \frac{2c}{D}\right] \tag{5}$$

The frequency bandwidth, Δf, determines the temporal resolution of the ramp response $\delta t = 1/(2\Delta f)$. As $f_{\max} \gg f_{\min}$, we get $\Delta f = f_{\max} - f_{\min} \approx f_{\max}$. Finally, the spatial resolution of the physical profile function is given by δx

$$\delta x = \frac{c\delta t}{2} = \frac{c}{4\Delta f} \approx \frac{c}{4f_{\max}} \tag{6}$$

Thus, the high frequency limit, $f_{\max}$, determines the spatial resolution of the profile function. If we choose $f_{\max}$ given by (5), we get

$$\delta x \approx \frac{c}{4f_{\max}} = \frac{D}{8} \tag{7}$$

Accordingly, to characterise complex shape objects, it is often necessary to increase $f_{\max}$ in order to obtain a better spatial resolution δx on the corresponding profile function.

In [18], we study the effect of frequency parameters on profile functions, namely the lower frequency limit f_{min}, the upper frequency limit f_{max} and the frequency step δf, and we conclude that the constraint on the lower limit of the frequency band, f_{min}, is the most difficult to fulfill in experiments. That is why, we have proposed some solutions to sort out this problem [19, 20].

2.3. Example of a PEC Sphere

To illustrate the process of getting the ramp profile function from the backscattered field, we present now the example of a perfectly electric conducting (PEC) sphere of diameter $D = 10\,cm$ in freespace (Fig. 2). For such value of D, the frequency band of investigation given by (5) is
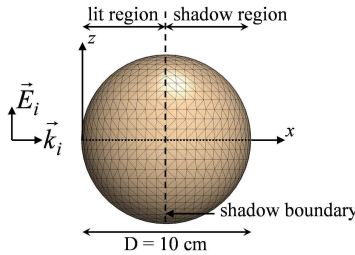

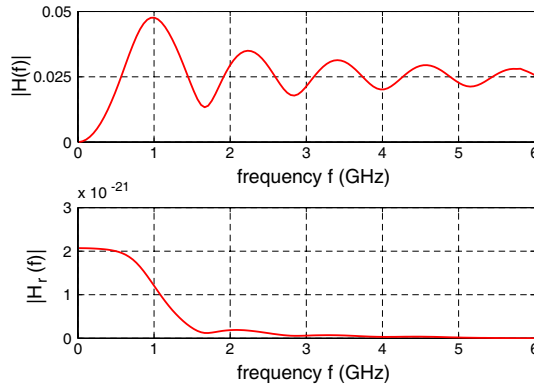**Figure 2.** Configuration of study for a PEC sphere of diameter $D = 10\,cm$.

Figure 3. Modulus of the transfer function $H(f)$ (upper) and the weighted transfer function $H_r(f)$ (lower) for a PEC sphere of diameter $D = 10\,cm$, in the frequency band $f = [15\,MHz; 6\,GHz]$ in monostatic configuration.

[15 MHz; 6 GHz]. An electromagnetic simulation software based on the Method of Moments [21] is used to calculate the transfer function $H(f)$ of this object in monostatic configuration and for an incident direction x. Fig. 3 (upper) plots the modulus of this transfer function, $H(f)$, while Fig. 3 (lower) presents the modulus of the weighted transfer function, $H_r(f) = H(f)/(j2\pi f)^2$. The main contribution is located in low frequencies on account of the weighting in $1/(j2\pi f)^2$. Next, the ramp response, $h_r(t)$, is calculated by IFT of $H_r(f)$ using (1), and the physical profile function, $A_p(x)$, is finally obtained from (4). Fig. 4 presents the ramp response, $h_r(t)$, (upper) and the corresponding physical profile function, $A_p(x)$, (lower) of the PEC sphere.

After selecting the useful part of $A_p(x)$, we compare, in Fig. 5, this physical profile function (solid line) with the geometrical profile function (dashed line), calculated analytically with (2): For the sphere, we get $A_g(x) = \pi x(D - x)$ for $0 \leq x \leq D$ and $A_g(x) = 0$ outside. The curves are very similar in the lit region ($x <= D/2 = 5$ cm). However, in the shadow region of the target ($x > D/2$), physical and geometrical profile functions differ. Indeed, in the lit region, the main contribution to the backscattered response at a given time t comes from the direct reflection of the incident wave on the surface of the PEC sphere at distance $x = ct/2$. On the contrary, in the shadow region, the contribution to the backscattered response comes from creeping waves traveling on the surface of the target, with a resulting additional delay in the response. This additional delay involves a spread of the physical profile function in the shadow region. In the
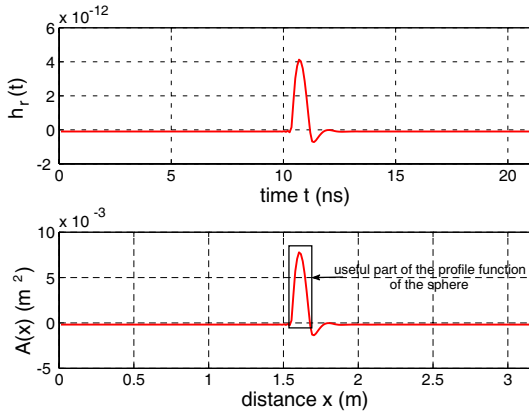

Figure 4. Ramp response $h_r(t)$ (upper) and physical profile function $A_p(x)$ (lower) of the PEC sphere.
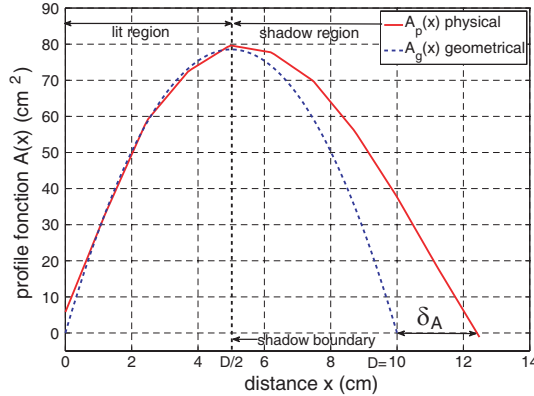
Figure 5. Comparison between physical $A_p(x)$ and geometrical $A_g(x)$ profile functions of the PEC sphere of diameter $D = 10$ cm.

case of the canonical PEC sphere, this spread, δ_A, is approximately equal to the path difference between the travel on the surface of the sphere (1/4 perimeter of the sphere) and the direct path (radius of the sphere): $\delta_A \approx \frac{D}{2}(\frac{\pi}{2} - 1) = 2.85$ cm. This difference might give inaccurate information on the target shape and must be compensated. One possible solution is to get the response in the opposite direction.

3. IMAGE RECONSTRUCTION FROM PROFILE FUNCTIONS

An analysis of profile functions of a target at several orientations can give information on its size and its approximate shape. This can be used directly as a signature for identification purposes. Furthermore, combining such responses so as to create a 3D image is an efficient means to represent the geometrical information on the target.

3.1. Young's Algorithm: "Approximate Limiting Surfaces"

A 3D image can be reconstructed from such multi-frequency scattering data at several look angles. Initially, Young [5] used ramp profile functions at 3 mutually orthogonal look angles and proposed an algorithm using a set of hyperbolic surfaces limiting the contour of the object for each viewing angle. Iteratively fitting geometrical parameters of these enclosing surfaces permits to obtain a final estimate of the object shape as the common volume of the set of 3 such

surfaces. This method has been later extended to non-orthogonal viewing angles [7, 22].

Unfortunately, this algorithm is limited to convex and individual objects [5]. That is why we propose a new image reconstruction algorithm enabling to reconstruct objects with arbitrary shape, as well as separated objects.

3.2. New Algorithm of Reconstruction

From profile functions obtained at 3 look angles, not necessarily orthogonal, we want to reconstruct the 3D shape of any target. To simplify the algorithm, we choose until now to use orthogonal
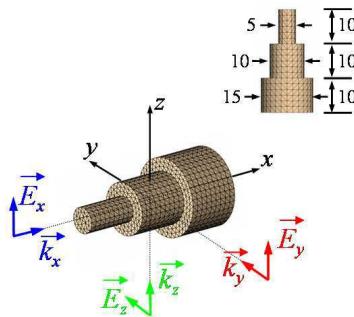

Figure 6. Configuration with 3 orthogonal directions for profile functions. Example of a stepcylinder (dimensions in cm).
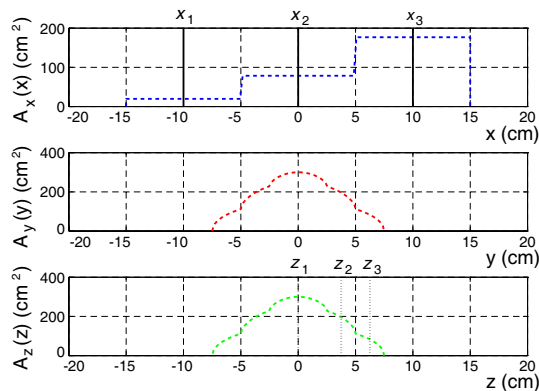

Figure 7. Geometrical profile functions of the stepcylinder for the 3 orthogonal look angles (x, y, z) defined in Fig. 6.

directions of observation (x, y, z). Without loss of generality, we illustrate the description of this algorithm with the example of a PEC stepcylinder (Fig. 6) and we use the geometrical profile functions of this object, $A_x(x)$, $A_y(y)$ and $A_z(z)$ (Fig. 7). Note that we choose to center the target and its resulting profile functions at the origin of the Cartesian coordinate system (x, y, z).

The new proposed algorithm consists of the following steps.

- First, we calculate a contribution given by the product of these 3 profile functions in each point of coordinates (x, y, z)

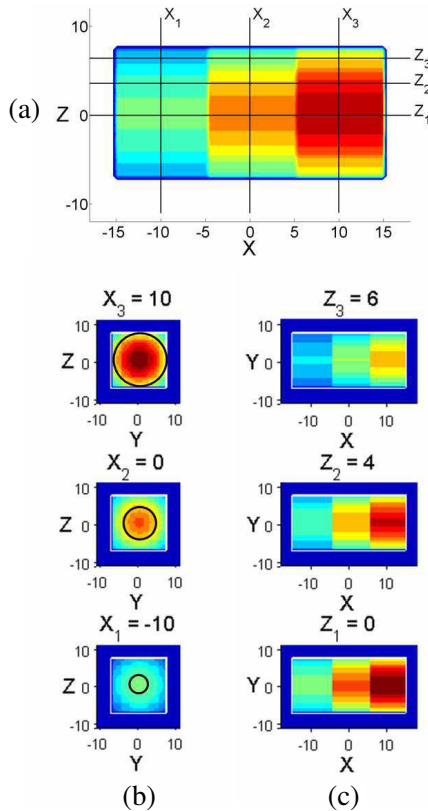$$A_{3D}(x, y, z) = A_x(x) \times A_y(y) \times A_z(z) \tag{8}$$

Figure 8. Representation of $A_{3D}(x, y, z)$ in various planes: (a) the xz cut-plane at $y = 0$, (b) 3 yz cut-planes for different x ($x_1 = -10$ cm, $x_2 = 0$ cm, $x_3 = 10$ cm) and (c) 3 xy cut-planes for different z ($z_1 = 0$ cm, $z_2 = 4$ cm, $z_3 = 6$ cm).

This 3D function A_{3D} can be considered as a weighting function accounting for the probability that a point (x, y, z) belongs to the initial object. A_{3D} is presented in Fig. 8: in (a) the cut-plane orthogonal to the direction y at $y = 0$, in (b) 3 sample cut-planes orthogonal to the direction x, at different positions $x_1 = -10\,\text{cm}$, $x_2 = 0\,\text{cm}$ and $x_3 = 10\,\text{cm}$, and in (c) 3 sample cut-planes orthogonal to the direction z, at different positions $z_1 = 0\,\text{cm}$, $z_2 = 4\,\text{cm}$ and $z_3 = 6\,\text{cm}$.

   - Next, we choose a scan direction, x, y or z. This choice is somewhat arbitrary, but best results are obtained with the most varying profile function, which is $A_x(x)$ in the case of the stepcylinder (Fig. 7).

   - Finally, we scan successive slices of the unknown object perpendicularly to the chosen direction, x for this example. For each cut-plane j, at position $x = x_j$, we know that the area of the target cross-section is equal to $A_x(x_j)$. Consequently, we select points (y, z) of this cut-plane with highest values of $A_{3D}(x_j, y, z)$, such as the resulting area of the object in the cut-plane x_j is equal to the value of the profile function $A_x(x_j)$

$$\sum_y \sum_z \delta y \delta z = A_x(x_j) \quad \text{such as} \quad (y, z) \in \text{object} \qquad (9)$$

where δy and δz are sampling step respectively in y and z.

   For an axisymetrical object as the stepcylinder of axis x, selected points in the yz cut-plane $x = x_j$ are located inside the circle of area equal to $A_x(x_j)$ (plotted in black in each cut-plane x_j of Fig. 8(b)). The reconstructed object is binary. Selected points belonging to the object are therefore given the value '1', while rejected points have the value '0'.

   Figure 10 presents the 3D image of the stepcylinder reconstructed with this new algorithm, using geometrical profile functions of Fig. 7. In this case of ideal profile functions and optimal scan direction x, the original object is accurately reconstructed. In order to quantitatively evaluate this new algorithm of reconstruction, we calculate the error between the reconstructed object and the initial object. The example of Fig. 9, for a particular cut-plane, shows that some pixels of the reconstructed object belong to the initial object, the "true" pixels, P_t, while the other ones do not belong to the initial object, the "false" pixels, P_f. $P_t + P_f$ is exactly the number of pixels of the reconstructed object. Next, the "missing" pixels, P_m, are pixels belonging to the initial object which are not selected in the reconstructed object. $P_t + P_m$ is exactly the number of pixels of the initial object. Finally, the "outside" pixels, P_o, correspond to pixels which belong neither to the initial object nor to the reconstructed object.
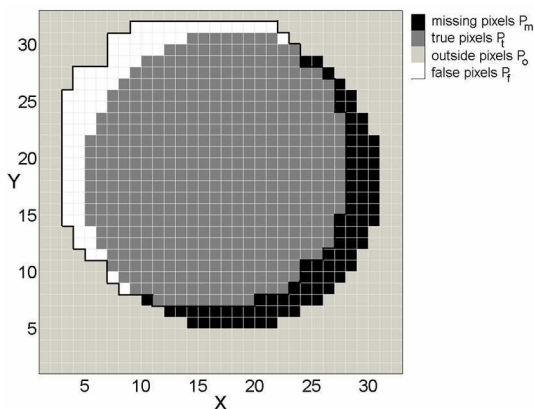
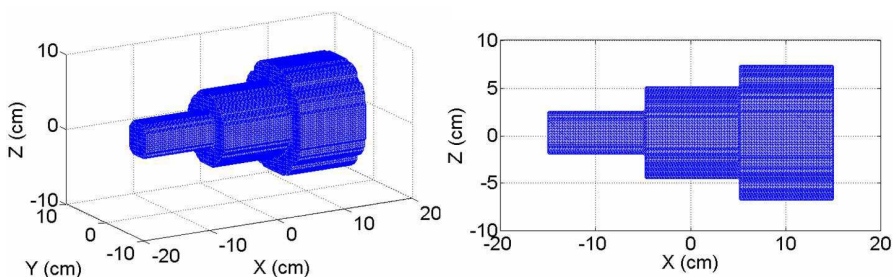**Figure 9.** Example of the initial and reconstructed objects in a cut-plane.

Figure 10. Reconstruction of the stepcylinder of Fig. 6 from the 3 geometrical profile functions of Fig. 7. Scan direction: x. Left: 3D view; Right: $(x\text{-}z)$ view (error 10%).

We choose to measure the error in each cut-plane j as the sum of false, $P_f(j)$, and missing, $P_m(j)$, pixels. The total error is thus calculated as the sum of errors for each cut-plane, normalized by the total number of pixels belonging to the initial object, P_{tot}.

$$E(\%) = 100 \times \frac{\sum_j (P_m(j) + P_f(j))}{P_{tot}} = 100 \times \frac{\sum_j (P_m(j) + P_f(j))}{\sum_j (P_m(j) + P_t(j))} \quad (10)$$

Using Eq. (10), the error is 10% for the reconstructed image of Fig. 10.

On the other hand, Fig. 11 presents the reconstructed image for the non-optimal scan direction z. In this case, we can see that the reconstructed stepcylinder is distorted, mainly the 1st and the 2nd
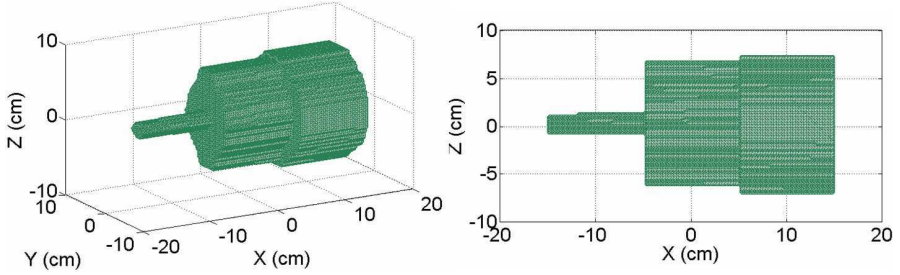
Figure 11. Reconstruction of the stepcylinder of Fig. 6 from the 3 geometrical profile functions of Fig. 7. Scan direction: z. Left: 3D view; Right: (x-z) view (error 30%).

cylinders: the error is 30%. From this result, we can conclude that the scan direction is very important to accurately reconstruct the shape of a target: Indeed, it is advised to choose the most varying profile function and/or the one which mostly differs from others.

Indeed, this algorithm seems very simple but the combined use of the 3 profile functions brings very strong information on the unknown object. This permits to obtain an accurate estimation of the target shape without any iteration, while Young's algorithm, considering independently limiting surfaces in each direction, needs several iterations to get an equivalent result [5]. Moreover, Young's algorithm needs good fitting skills to perform well. Therefore, we invite the reader to compare our results to the literature [5, 22], instead of performing a sub-optimal reconstruction.

4. RESULTS OF IMAGING WITH RAMP PROFILE FUNCTIONS

After presenting our new algorithm in the "ideal" case of geometrical profile functions, we now consider the realistic case of physical profile functions obtained from simulated transient responses of targets. As explained in Section 2, the field backscattered by a target is calculated for 3 incident directions using FEKO [21], in the required frequency band given by (5), then ramp responses and physical profile functions are calculated using (1) and (4).

We first consider the previous stepcylinder in the same configuration with 3 directions of observation (x, y, z) (Fig. 6). Physical profile functions, $A_x(x)$, $A_y(y)$ and $A_z(z)$ are compared to geometrical ones in Fig. 12. Differences between geometrical and physical profile functions are mainly due to the shadow region effect.
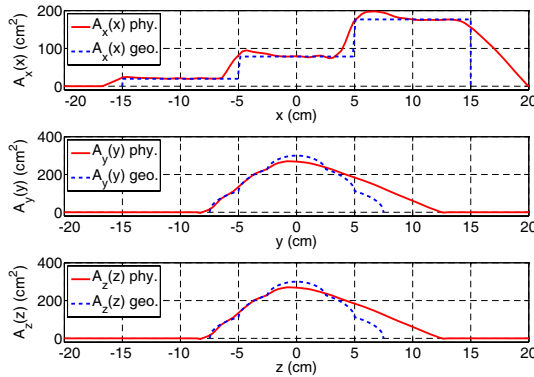
Figure 12. Comparison of physical and geometrical profile functions of the stepcylinder for the 3 orthogonal look angles (x, y, z) defined in Fig. 6 (frequency band $= [5\,\text{MHz}; 8\,\text{GHz}]$).
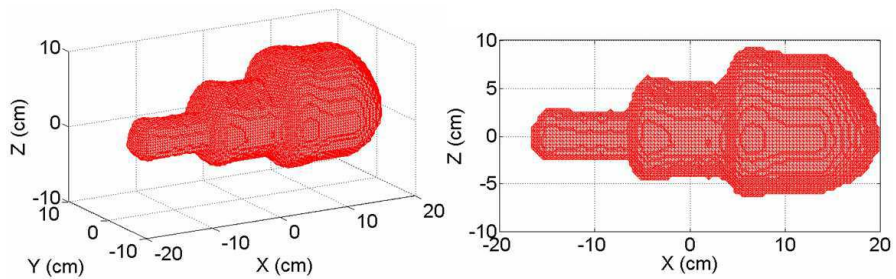

Figure 13. Reconstruction of the stepcylinder of Fig. 6 from the 3 physical profile functions of Fig. 12. Scan direction: x. Left: 3D view; Right: $(x\text{-}z)$ view (error 34%).

We apply our new algorithm to reconstruct the 3D image, with the scan direction x. The resulting image (Fig. 13) is distorted as compared to the original object, with an error equal to 34%, yet this result is still acceptable in the context of low frequency imaging where the goal is not to reconstruct a high resolution image but to identify a target from its approximate shape.

We now consider the example of an asymmetric object (Fig. 14(a)). Fig. 14(b) compares geometrical and physical profile functions in x, y and z directions. Once again, differences mainly exist in the shadow region, with the spreading of physical profile functions. Fig. 14(c) shows that geometrical profile functions permit an accurate 3D reconstruction, using scan direction x ($E = 1\%$). On
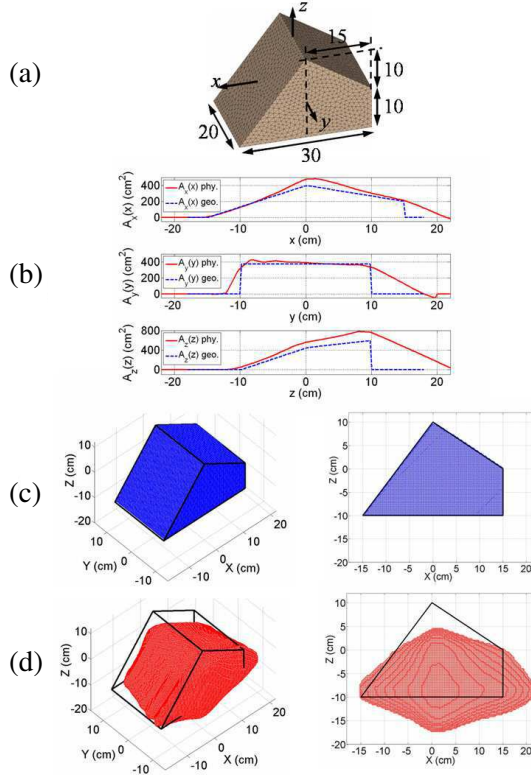
Figure 14. Configuration of study for a non-symmetric object: (a) object shape (dimensions in cm), (b) comparison of physical and geometrical profile functions and 3D reconstructed images from geometrical (c) ($E = 1\%$) and physical (d) ($E = 58\%$) profile functions with scan direction x.

the contrary, physical profile functions result in a strongly distorted image, Fig. 14(d), because of the shadow effect ($E = 58\%$). However, we recall that our goal is to identify the target and not to reconstruct a high resolution image.

As we said before, Young's algorithm can be used only for convex and single object [5]. On the contrary, we further want to show that this new algorithm can reconstruct non-convex objects and even separated objects. We first consider the example of a continuous non-convex PEC object, a cylinder with circular cross-sections of different diameters. Fig. 15 presents respectively (a) the object geometry, (b) physical profile functions for 3 orthogonal look angles and (c)
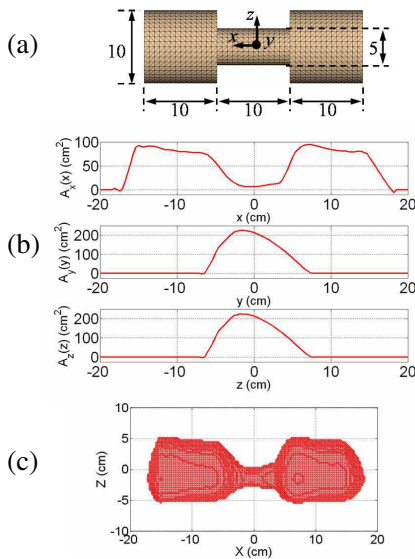
Figure 15. Configuration of study for a non-convex stepcylinder: (a) object shape (dimensions in cm), (b) physical profile functions and (c) 3D reconstructed image with scan direction x (error 37%).
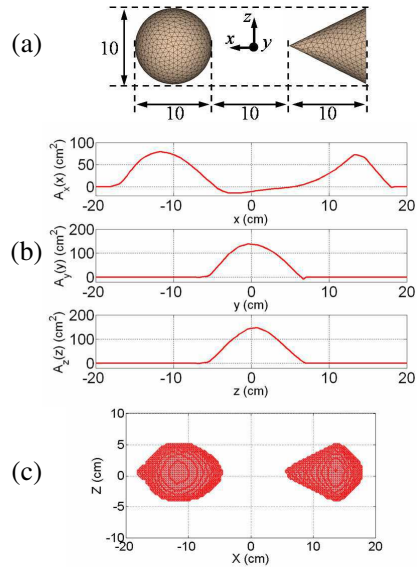
Figure 16. Configuration of study for 2 separated objects (sphere + cone): (a) objects shapes (dimensions in cm), (b) physical profile functions and (c) 3D reconstructed image with scan direction x (error 40%).

the 3D reconstructed image with scan direction x. The object is reasonably reconstructed and easily identifiable, even if distorted in shadow regions. The error is 37%.

Second, we consider two separated PEC objects, a cone and a sphere. Fig. 16 presents respectively (a) the objects, (b) physical profile functions for 3 orthogonal look angles and (c) the 3D reconstructed image with scan direction x. Once again, both objects are reasonably reconstructed and easily identifiable ($E = 40\%$). In [23], we determine the limit of separation provided by our new algorithm, using the example of 2 PEC spheres.

Both examples allow us to confirm that this new algorithm of reconstruction overcomes the inability of the "approximate limiting surfaces" algorithm to deal with non-convex and/or separated objects.

5. CONCLUSION AND PERSPECTIVES

We have presented a low frequency radar tri-dimensional imaging method using ramp responses of targets. The ramp response technique has several advantages. First, despite a poorer resolution than high frequency imaging, this method can be useful for the characterization of stealthy or buried targets. Second, contrary to other types of 3D imaging techniques, which require target radar echo measurements at multiple antenna positions to reconstruct an accurate target image, the ramp response technique usually needs no more than 3 viewing angles to generate an image. Third, this method is relatively insensitive to noise [22]. Finally, its main advantage comes from its easiness: indeed, from the transfer function of the target backscattering, a simple division by the squared frequency and an inverse Fourier transform permit to know the approximate profile of a radar target.

The previously Young's algorithm of 3D reconstruction from ramp responses uses a set of hyperbolic surfaces limiting the contour of the object for each viewing angle independently. An iterative fitting of geometrical parameters of these enclosing surfaces permits to obtain an estimate of the final image as the volume common to the three set of such surfaces. Consequently, this technique is limited to single convex objects. On the contrary, the new algorithm introduced in this paper manages to exploit the information more effectively, by using simultaneously the 3 profile functions through a 3D "weighting" function in order to select each pixel of the reconstructed object. Consequently, this algorithm is able to reconstruct the global shape of non-convex and/or separated objects, and to directly obtain a satisfactory estimate of these objects. To overtake the inherent limitation caused by shadowing effects in the ramp response, this method can be improved by a further iterative process with a priori information on the target and the addition of other view angles. Moreover, the use of non-orthogonal observing directions results in a distortion of the reconstruct target. In future works, this imaging reconstruction method will be extended to arbitrary, non-orthogonal, look angles.

REFERENCES

1. Colton, D. and R. Kress, *Inverse Acoustic and Electromagnetic Scattering Theory*, 2nd editon, Series: Applied Mathematical Sciences, Vol. 93, Springer-Verlag, 1998.

2. Solimene R., A. Brancaccio, R. Di Napoli, and R. Pierri, "3D sliced tomographic inverse scattering experimental results," *Progress In Electromagnetics Research*, Vol. 105, 1–13, 2010.

3. Chavent, G. and P. C. Sabatier, *Proceedings of Inverse Problems of Wave Propagation and Diffraction*, Vol. 486, Lecture Notes in Physics, Springer, Aix-les-Bains, France, 1997.

4. Bojarski, N. N., *Three-dimensional Electromagnetic Short Pulse Inverse Scattering*, Syracuse University, Res. Corp., Syracuse, NY, Feb. 1967.

5. Young, J. D., "Radar imaging from ramp response signatures," *IEEE Trans. Ant. Prop.*, Vol. 24, 276–282, May 1976.

6. Kennaugh, E. M. and D. L. Moffatt, "Transient and impulse response approximations," *Proceedings of the IEEE*, Vol. 53, 893–901, 1965.

7. Shubert, K. A., J. D. Young, and D. L. Moffatt, "Synthetic radar imagery," *IEEE Trans. Ant. Prop.*, Vol. 25, 477–483, Jul. 1977.

8. Moffatt, D. L., "Ramp response radar imagery spectral content," *IEEE Trans. Ant. Prop.*, Vol. 29, 399–401, Mar. 1981.

9. Nag, S. and L. Peters, Jr., "Radar images of penetrable targets generated from ramp profile functions," *IEEE Trans. Ant. Prop.*, Vol. 49, 32–40, Jan. 2001.

10. Chen, C.-C. and L. Peters, Jr., "Radar scattering and target imaging obtained using ramp-response techniques," *Antennas and Propagation Magazine*, Vol. 49, No. 3, 13–27, Jun. 2007.

11. Moffatt, D. L., J. D. Young, A. A. Ksienski, H.-C. Lin, and C. M. Rhoads, "Transient response characteristics in identification and imaging," *IEEE Trans. Ant. Prop.*, Vol. 29, 192–204, Mar. 1981.

12. Nag, S. and L. Peters, Jr., "Ramp response signatures of dielectric targets, especially land mines," *Geoscience and Remote Sensing Symposium Proceedings*, Vol. 1, 213–315, Jul. 1998.

13. Chen, C.-C. and L. Peters, Jr., "Ramp response signatures for UXOs," *Geoscience and Remote Sensing Symposium Proceedings*, Vol. 4, 1436–1438, 2000.

14. Young, J. D., "Target imaging from multiple frequency radar returns," Ph.D. Dissertation, The Ohio State University,

Columbus, Jun. 1971.

15. Nag, S., "Ramp response signatures of dielectric scatterers," Ph.D. Dissertation, The Ohio State University, Columbus, Dec. 1999.

16. Zhang, X. M., W. Lib, and G. R. Liu, "A new technique in ramp response for acoustic imaging of underwater objects," *Applied Acoustics*, Vol. 63, 453–465, 2002.

17. Li, W., G. R. Liu, and V. K. Varadan, "Acoustical imaging of underwater objects using the bistatic ramp response signals," *IOP, Smart Mater. Struct.*, Vol. 13, 169–174, 2004.

18. Chauveau, J. and N. de Beaucoudrey, "Ramp response radar imaging: Analysis of frequency parameters," *European Microwave Week 2010 (EuMW)*, Paris, France, Sep. 26–Oct. 1, 2010.

19. Chauveau, J. and N. de Beaucoudrey, "Characterization of details of large targets with the low-frequency ramp response technique," *IEEE International Symposium on Antennas and Propagation and CNC/USNC/URSI Radio Science Meeting*, Toronto, Ontario, Canada, Jul. 11–17, 2010.

20. Chauveau, J., N. de Beaucoudrey, and J. Saillard, "Radar target imaging from ramp responses using low frequency extrapolation," *Progress In Electromagnetics Research Symposium Abstracts*, 18–21, Moscow, Russia, Aug. 18–21, 2009.

21. FEKO, Software of Electromagnetic Simulations, http://www.feko.info.

22. Tsao, S.-J. J., "Image reconstruction using ramp response signatures," Ph.D. Dissertation, The Pennsylvania State University, May 1985.

23. Chauveau, J. and N. de Beaucoudrey, "Low frequency imaging of separated objects using the ramp response technique," *IEEE International Symposium on Antennas and Propagation and CNC/USNC/URSI Radio Science Meeting*, Toronto, Ontario, Canada, Jul. 11–17, 2010.